

Non-stationary Spatial Modeling Using Fractional SPDEs

Elling Svee^a, Geir-Arne Fuglstad^a

^aNorwegian University of Science and Technology, Alfred Getz' vei 1, 7034, Trondheim, Norway

ARTICLE INFO

Keywords:

- Spatially varying anisotropy
- Fractional smoothness
- SPDE approach
- Gaussian Markov random fields
- Ocean salinity
- Precipitation

ABSTRACT

We construct a Gaussian random field (GRF) that combines fractional smoothness with spatially varying anisotropy. The GRF is defined through a stochastic partial differential equation (SPDE), where the range, marginal variance, and anisotropy vary spatially according to a spectral parametrization of the SPDE coefficients. Priors are constructed to reduce overfitting in this flexible covariance model, and parameter estimation is done with an efficient gradient-based optimization approach that combines automatic differentiation with sparse matrix operations. In a simulation study, we investigate how many observations are required to reliably estimate fractional smoothness and non-stationarity, and find that one realization containing 500 observations or more is needed in the scenario considered. We also find that the proposed penalization prevents overfitting across varying numbers of observation locations. Two case studies demonstrate that the relative importance of fractional smoothness and non-stationarity is application dependent. Non-stationarity improves predictions in an application to ocean salinity, whereas fractional smoothness improves predictions in an application to precipitation. Predictive ability is assessed using mean squared error and the continuous ranked probability score. In addition to prediction, the proposed approach can be used as a tool to explore the presence of fractional smoothness and non-stationarity.

1. Introduction

Gaussian random fields (GRFs) are a common tool for spatial modeling in fields such as environmental sciences and ecology (Cressie and Wikle, 2011; Banerjee et al., 2015). Isotropic covariance models are widely used, and the Matérn family of covariance functions (Stein, 1999) is an appealing choice because it has three interpretable parameters that can be controlled separately: 1) marginal variance, 2) spatial range, and 3) smoothness. However, in many applications, isotropy and stationarity are unrealistic assumptions. This has motivated work on more flexible covariance structures (Sampson, 2010; Schmidt and Guttorm, 2020), as well as approaches that enable efficient inference for spatial models (Heaton et al., 2019). In this paper, we extend the popular *SPDE approach* (Lindgren et al., 2011, 2022) to simultaneously incorporate both spatially varying anisotropy and fractional smoothness, and use the extended model to explore the relative importance of these for two datasets.

Several approaches have been proposed to model non-stationary spatial processes. One prominent class of methods is the deformation approach, where the spatial domain is transformed through a bijective mapping such that the process appears stationary in the transformed space (Sampson and Guttorm, 1992; Damian et al., 2001; Schmidt and O'Hagan, 2003). Another strategy relies on convolution-based constructions, which represent the spatial process as a smoothed integral of a latent process, allowing the covariance structure to vary across space (Higdon, 1998; Paciorek and Schervish, 2006). Covariate-driven models offer an alternative, incorporating spatially varying covariates directly

✉ elling.svee@ntnu.no (E. Svee); geir-arne.fuglstad@ntnu.no (G. Fuglstad)
<https://ellingsvee.github.io/> (E. Svee); <https://www.ntnu.no/ansatte/geir-arne.fuglstad> (G. Fuglstad)
ORCID(s): 0009-0008-4225-964X (E. Svee); 0000-0003-4995-2152 (G. Fuglstad)

into the covariance function to capture heterogeneity (Neto et al., 2014; Risser and Calder, 2015). Notably, several of these approaches have associated software implementations, such as the local covariance models provided by Risser and Calder (2017); Risser and Turek (2020). However, while the methods give considerable flexibility, they use dense covariance matrices which often come with a substantial computational cost.

The SPDE approach proposed by Lindgren et al. (2011) provides an efficient alternative by approximating non-stationary GRFs using sparse precision matrices. Ingebrigtsen et al. (2015) applied the approach to model annual precipitation in southern Norway, while Fuglstad et al. (2015a) incorporated spatially varying anisotropy. Fuglstad et al. (2015b) demonstrated that non-stationary models can improve predictive performance, but also emphasized the importance of carefully controlling model flexibility to avoid overfitting. Another important extension is the rational approximation for fractional SPDEs introduced by Bolin and Kirchner (2020). This enables GRFs with arbitrary smoothness parameters, overcoming the limitation of the original SPDE formulation being restricted to a limited set of smoothness values. The example in Bolin and Kirchner (2020, Section 7) combined non-stationary range and variance with a fractional smoothness parameter, but assumed isotropy.

This paper extends existing work on non-stationary fractional SPDE models by incorporating non-stationarity in the anisotropy. The result is a more flexible class of models capable of capturing a wider range of spatial processes. A key challenge in non-stationary SPDE-based modeling is practical inference (Lindgren et al., 2022), and it is well established that penalizing the flexibility of non-stationary components through appropriate priors is essential (Fuglstad et al., 2019). We therefore develop priors for both stationary and non-stationary parameters. To obtain gradients during parameter estimation, we differentiate the log-likelihood using *automatic differentiation* (AD). Compared to finite-difference approaches, this technique scales well with the number of parameters, making it ideal for non-stationary models.

The proposed model is assessed and compared to simpler alternatives through a simulation study. We investigate the relative importance of non-integer smoothness and non-stationarity, and how this depends on prior specification and data availability. Our primary focus is on predictive performance, measured using the *root mean square error* (RMSE) and the *continuous ranked probability score* (CRPS). The parameter estimates are evaluated through their bias. We also investigate the importance of non-stationarity versus fractional smoothness in two case studies: 1) emulation of a numerical model describing the ocean salinity in Trondheimsfjorden (SINTEF, 1987; Slagstad and McClimans, 2005), and 2) analysis of data from a climate reanalysis model describing the average summer precipitation over the conterminous U.S. (Genton and Kleiber, 2015). These are both data-rich cases where we emulate output from numerical models, and where we expect including non-stationarity or a fractional smoothness to enhance model performance

In Section 2 we present the proposed SPDE model, detailing its discretization and how we approximate the fractional smoothness. Section 3 specifies our choice of parameterization and priors for the stationary and non-stationary parameters. Then in Section 4, we outline the hierarchical modeling framework used for inference, and explain how we apply AD to compute gradients during parameter estimation. The performance of the model is evaluated through a simulation study in Section 5 and case studies in Section 6. Lastly, the paper concludes with Section 7, summarizing our main results and outlining potential directions for future research. A Python implementation of the model can be found at <https://github.com/ellingsvee/FracNonStatSPDE>.

2. Specifying and discretizing the covariance structure

2.1. Covariance model

Inspired by Bolin and Kirchner (2020); Bolin et al. (2024), we consider a GRF $u(\cdot)$ on the bounded domain $\mathcal{D} \subset \mathbb{R}^2$. Its covariance structure is described through the SPDE

$$\begin{cases} (\kappa(s) - \nabla \cdot \mathbf{H}(s) \nabla)^\beta u(s) = \tau(s) \mathcal{W}(s), & s \in \mathcal{D}, \\ (\mathbf{H}(s) \nabla u(s)) \cdot \mathbf{n}(s) = 0, & s \in \partial \mathcal{D}, \end{cases} \quad (1)$$

where $\mathcal{W}(\cdot)$ is Gaussian white noise, $\mathbf{n}(\cdot)$ is the outwards normal vector, $\kappa(\cdot)$ and $\tau(\cdot)$ are positive functions, and $\mathbf{H}(\cdot)$ is a spatially varying positive-definite 2×2 matrix. For the SPDE to give a GRF with finite variance, we need $\beta > 1/2$. In this paper, we choose parametrizations of $\kappa(\cdot)$, $\tau(\cdot)$ and $\mathbf{H}(\cdot)$ that ensure that these functions are smooth on $\bar{\mathcal{D}} = \mathcal{D} \cup \partial\mathcal{D}$, $\kappa(\cdot) \geq \kappa_1 > 0$, and that the smallest eigenvalue of $\mathbf{H}(\cdot)$ is greater than some $\lambda_1 > 0$. These conditions are stricter than necessary conditions for a solution to exist, and interested readers can see milder conditions in Bolin and Kirchner (2020).

For stationary $\kappa(\cdot) \equiv \kappa_0$, $\mathbf{H}(\cdot) \equiv \mathbf{H}_0$ and $\tau(\cdot) = \tau_0$, Equation (1) gives approximately rise to a Matérn covariance function with geometric anisotropy,

$$c(\mathbf{h}) = \frac{\sigma_0^2}{2^{\nu-1}\Gamma(\nu)} \left(\kappa_0 \left\| \mathbf{H}_0^{-1/2} \mathbf{h} \right\| \right)^\nu K_\nu \left(\kappa_0 \left\| \mathbf{H}_0^{-1/2} \mathbf{h} \right\| \right), \quad \mathbf{h} \in \mathbb{R}^2. \quad (2)$$

\mathbf{h} is a displacement vector, $\nu = 2\beta - 1$ is the smoothness, $K_\nu(\cdot)$ is the modified Bessel function of the second kind with order ν , and the marginal standard deviation is

$$\sigma_0 = \sqrt{\frac{\Gamma(2\beta-1)}{4\pi\Gamma(2\beta)}} \frac{\tau_0}{\kappa_0^{2\beta-1} |\mathbf{H}_0|^{1/4}}.$$

As discussed in Lindgren et al. (2011), the effect of the boundary can be reduced by extending the size of the domain outside the area of interest. When $\kappa(\cdot)$ and $\mathbf{H}(\cdot)$ are non-stationary, they affect both marginal variance and correlation structure. We therefore choose to introduce the positive and smooth function $\sigma(\cdot)$, and let

$$\tau(\mathbf{s}) = \sigma(\mathbf{s}) \sqrt{4\pi \frac{\Gamma(2\beta)}{\Gamma(2\beta-1)}} \kappa(\mathbf{s})^{2\beta-1} |\mathbf{H}(\mathbf{s})|^{1/4}, \quad \mathbf{s} \in \mathcal{D}. \quad (3)$$

The aim of this is to reduce the dependence of marginal variance on $\kappa(\cdot)$ and $\mathbf{H}(\cdot)$, and to introduce a separate function $\sigma(\cdot)$ that controls marginal standard deviation. The decoupling is not exact for spatially varying parameters, but it would decouple correlation and marginal variance exactly (up to boundary conditions) for the case of constant coefficients.

In Fuglstad et al. (2015a), the spatially varying positive definite matrix $\mathbf{H}(\cdot)$ is described through a baseline isotropic component and a vector field describing the direction and strength of extra dependence. However, this leads to an invariance to multiplying the vector field by the factor -1 . We instead use the parameterization recently proposed by Llamazares-Elias et al. (2024)

$$\mathbf{H} = \cosh(\|\mathbf{v}\|) \mathbf{I} + \frac{\sinh(\|\mathbf{v}\|)}{\|\mathbf{v}\|} \begin{bmatrix} v_x & v_y \\ v_y & -v_x \end{bmatrix}, \quad (4)$$

where \mathbf{v} is a spatially varying vector field. For ease of notation, we have suppressed the dependence of location \mathbf{s} . This parameterization is bijective, and \mathbf{H} will always be a positive definite matrix with determinant 1.

Let correlation range be defined as the distance where correlation is approximately 0.13. Denote the eigenpairs of \mathbf{H} at a fixed location as $(\lambda_{\max}, \mathbf{v}_{\max})$ and $(\lambda_{\min}, \mathbf{v}_{\min})$, where $\lambda_{\max} \geq \lambda_{\min}$. Then the largest correlation $\rho_{\max} = \sqrt{8\nu\lambda_{\max}/\kappa}$ is largest in the direction \mathbf{v}_{\max} , and smallest in the direction \mathbf{v}_{\min} where it is $\rho_{\min} = \sqrt{8\nu\lambda_{\min}/\kappa}$. By Llamazares-Elias et al. (2024, Section 2), the eigenvalues of \mathbf{H} are

$$\lambda_{\max} = \exp\{\|\mathbf{v}\|\} \quad \text{and} \quad \lambda_{\min} = \exp\{-\|\mathbf{v}\|\}.$$

This gives rise to interpretable parameters: 1) geometric average of minimum and maximum ranges $\rho = \sqrt{\rho_{\max}\rho_{\min}} = \sqrt{8\nu/\kappa}$, 2) ratio between maximum and minimum ranges $a = \rho_{\max}/\rho_{\min} = \exp(2\|\mathbf{v}\|)$, and 3) angle ψ between direction with max correlation and the x -axis, defined as $(\cos 2\psi, \sin 2\psi) = \mathbf{v}/\|\mathbf{v}\|$ with $\psi \in (-\pi/2, \pi/2]$. Figure 1 illustrates an iso-correlation curve, showing relation between \mathbf{v} , the angle ψ and the and the correlation ranges.

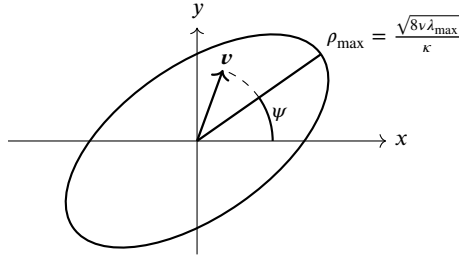


Figure 1: Illustrating the relation between the parameterized vector v and the iso-correlation curve at a fixed location. λ_{\max} denotes the maximum eigenvalue of \mathbf{H} . The angle ψ of the anisotropy is half of the angle of v .

In summary, we have a Whittle-Matérn covariance structure, which reduces to approximately Matérn with geometric anisotropy for constant coefficients $\kappa(\cdot) \equiv \kappa_0$, $\mathbf{H}(\cdot) \equiv \mathbf{H}_0$, and $\sigma(\cdot) \equiv \sigma_0$. Isotropy is achieved by setting $\mathbf{H}_0 = \mathbf{I}$. In the stationary case, one can see that the resulting covariance function is overparametrized since τ_0 is superfluous. Due to the parameterization of $\mathbf{H}(\cdot)$ in Equation (4), the number of parameters required to describe \mathbf{H}_0 reduces from three to one, meaning the τ_0 is necessary. For the non-stationary GRF, we assume latent models where $\log \kappa(\cdot)$, $\log \sigma(\cdot)$, $v_x(\cdot)$ and $v_y(\cdot)$ are independent GRFs. Log-transformations are here used to ensure that $\kappa(\cdot)$ and $\sigma(\cdot)$ remain positive. The choice of latent model or prior is discussed in Sections 3 and 4. The associated interpretable parameters, $\rho(\cdot)$, $a(\cdot)$ and $\psi(\cdot)$, are then also spatially varying, but their interpretation is not directly corresponding to their stationary counterpart when the covariance structure is not stationary.

2.2. Discretization for efficient computations

2.2.1. Non-fractional SPDE

We follow Lindgren et al. (2011) and consider a triangular mesh of the domain \mathcal{D} with m vertices. We define the piecewise linear basis functions $\{\varphi_i\}_{i=1}^m$. These equal one on their corresponding vertex and zero on all others, together forming a compactly supported and finite-dimensional function space. The solution of SPDE in Equation (1) is approximated by the GRF

$$\tilde{u}(s) = \sum_{i=1}^m w_i \varphi_i(s), \quad s \in \mathcal{D}, \quad (5)$$

where $\mathbf{w} = (w_1, \dots, w_m)^T \sim \mathcal{N}(\mathbf{0}, \mathbf{Q}^{-1})$. We approximate the precision matrix \mathbf{Q} using a *finite element method* (FEM).

The triangulation \mathcal{T} is a set of triangles $T \subset \mathbb{R}^2$. For $T \in \mathcal{T}$, let $\langle f, g \rangle_T = \int_T f(s)g(s)ds$ and let s_T denote the centroid of T . Considering first $\beta = 1$ and following the steps in Lindgren et al. (2011), the FEM gives rise to a finite dimensional $m \times m$ linear system

$$\mathbf{L}\mathbf{w} \stackrel{\text{def}}{=} (\mathbf{C}_{\kappa^2} + \mathbf{G})\mathbf{w} \stackrel{d}{=} \mathbf{C}_{\tau^2}^{1/2}\mathbf{z}, \quad \mathbf{z} \sim \mathcal{N}(\mathbf{0}, \mathbf{I}), \quad (6)$$

where $\stackrel{d}{=}$ denotes equality in distribution. The mass-matrices are computed using mass-lumping

$$(\mathbf{C}_f)_{ij} = \begin{cases} \sum_{T \in \mathcal{T}} f(s_T) \langle 1, \varphi_i \rangle_T \approx \int_D f(s) \varphi_i(s) ds, & i = j, \\ 0, & i \neq j, \end{cases} \quad \text{for } f(\cdot) \in \{\kappa^2(\cdot), \tau^2(\cdot)\},$$

and let \mathbf{C} denote the matrix with $f(\cdot) \equiv 1$. The stiffness matrix \mathbf{G} is computed as

$$\mathbf{G}_{ij} = \sum_{T \in \mathcal{T}_h} \langle \nabla \varphi_i, \mathbf{H}(s_T) \nabla \varphi_j \rangle_T \approx \int_D (\nabla \varphi_i(s))^T (\mathbf{H}(s) \varphi_j(s)) ds.$$

Solving Equation (6) for \mathbf{w} we obtain $\mathbf{Q}_1 = \mathbf{L}^T \mathbf{C}_{\tau^2}^{-1} \mathbf{L}$. Following the iterative approach from (Lindgren et al., 2011, Appendix 4), we can also determine the precisions for higher integer values of β , giving

$$\begin{cases} \mathbf{Q}_1 = \mathbf{L}^T \mathbf{C}_{\tau^2}^{-1} \mathbf{L}, & \beta = 1, \\ \mathbf{Q}_\beta = \mathbf{L}^T \mathbf{C}^{-1} \mathbf{Q}_{\beta-1} \mathbf{C}^{-1} \mathbf{L}, & \beta = 2, 3, \dots \end{cases} \quad (7)$$

The resulting precision matrices are sparse, but includes more and more non-zero terms for increasing values of β .

2.2.2. Fractional SPDE

The solution for non-integer β is approximated using the rational SPDE approach. We refer to Bolin and Kirchner (2020) for the rigorous details, and instead focus on presenting the main ideas. Equation (6) suggests that the discrete version of the operator $L = (\kappa(\cdot) - \nabla \cdot \mathbf{H}(\cdot) \nabla)$ is $\mathbf{C}^{-1} \mathbf{L}$ for the coefficients of the FEM basis. This means that in Equation (6), $\mathbf{C}^{-1} \mathbf{L}$ would map between the coefficients of the solution \mathbf{w} and the coefficients $\mathbf{C}^{-1} \mathbf{C}_{\tau^2}^{1/2} \mathbf{z}$ of the right hand side. Bolin and Kirchner (2020) argue that one should work with the operator L^{-1} , defined in the sense that $f = L^{-1}g$ solves $Lf = g$ under the no flow boundary conditions. The inverse operator behaves better than the original operator since the eigenvalues are bounded from above and belong to some interval $J = (0, \lambda_0^{-1}]$. Consequently, the problem reduces to finding a computationally efficient approximation of $(\mathbf{C}^{-1} \mathbf{L})^{-\beta}$ for $\beta > 1/2$.

Consider the real function $r(x) = x^\beta$ for $x \in J$, and let $k_\beta = \max\{1, \lfloor \beta \rfloor\}$. We choose an approximation of the form $\tilde{r}(x) = P_R(x)P_L(x)^{-1}$ for $x \in J$, where $P_R(x) = \sum_{i=0}^k c_i x^i$, $P_L(x) = x^{k_\beta} \sum_{i=0}^{k+1} b_i x^i$, and k is the order of the rational approximation. It is called a rational approximation because both the denominator and the numerator are polynomials. The coefficients b_0, \dots, b_{k+1} and c_0, \dots, c_k are chosen according to the Clenshaw–Lord Chebyshev–Padé algorithm (Baker and Graves-Morris, 1996). We can then express

$$r(x^{-1}) \approx \tilde{r}(x^{-1}) = \left(\sum_{i=0}^k c_i x^{k-i} \right) \left(x^{k_\beta-1} \sum_{i=0}^{k+1} b_i x^{k+1-i} \right)^{-1}, \quad x^{-1} \in J.$$

This approximation is constructed for a real function, but can be extended to an approximation for symmetric positive-definite matrices. To improve stability, Bolin and Kirchner (2020) in the stationary and non-isotropic case suggest rescaling \mathbf{L} by a factor κ_0^{-2} . For our non-stationary model we apply a rescaling $\mathbf{K} = \kappa_{\min}^{-2} \mathbf{L}$ with $\kappa_{\min} = \min_{s \in D} \kappa(s)$. This does not guarantee the same bounds on the eigenvalues as in Bolin and Kirchner (2020), but we in practice found the selected rescaling to be sufficiently stable. Inserting the rescaled $\mathbf{C}^{-1} \mathbf{K}$ into the formulas for P_R and P_L gives $(\mathbf{C}^{-1} \mathbf{L})^{-\beta} \approx \mathbf{P}_R \mathbf{P}_L^{-1}$, where $\mathbf{P}_L = \kappa_{\min}^{2(k_\beta+k)} (\mathbf{C}^{-1} \mathbf{K})^{k_\beta-1} \sum_{i=0}^{k+1} b_i (\mathbf{C}^{-1} \mathbf{K})^{k+1-i}$ and $\mathbf{P}_R = \kappa_{\min}^{2(k-1)} \sum_{i=0}^k c_i (\mathbf{C}^{-1} \mathbf{K})^{k-i}$. We may then write the approximate solution for the FEM basis coefficients as

$$\mathbf{w} \stackrel{d}{=} (\mathbf{C}^{-1} \mathbf{L})^{-\beta} \mathbf{C}^{-1} \mathbf{C}_{\tau^2}^{1/2} \mathbf{z} \approx \mathbf{P}_R \mathbf{P}_L^{-1} \mathbf{C}^{-1} \mathbf{C}_{\tau^2}^{1/2} \mathbf{z}, \quad \mathbf{z} \sim \mathcal{N}(\mathbf{0}, \mathbf{I}).$$

This can be more compactly written as $\mathbf{w} = \mathbf{P}_R \tilde{\mathbf{w}}$ and $\tilde{\mathbf{w}} \sim \mathcal{N}(\mathbf{0}, \tilde{\mathbf{Q}}^{-1})$, where $\tilde{\mathbf{Q}} = \mathbf{P}_L^T \mathbf{C} \mathbf{C}_{\tau^2}^{-1} \mathbf{C} \mathbf{P}_L$. To maintain a consistent notation across fractional and non-fractional smoothnesses, let $\mathbf{P}_R = \mathbf{I}$ and $\mathbf{P}_L = (\mathbf{C}^{-1} \mathbf{L})^\beta$ for $\beta \in \mathbb{N}$.

3. Parametrization and prior for covariance structure

Our GRF distribution depends on the smoothness v and the four non-stationary parameters $\log \kappa(\cdot)$, $\log \sigma(\cdot)$, $v_x(\cdot)$ and $v_y(\cdot)$. We choose to parameterize the functions on a rectangular domain $D = (A_1, A_2) \times (B_1, B_2) \subset \mathbb{R}^2$. If the area of interest is not rectangular, one could choose a rectangular domain covering the area of interest. Each non-stationary parameter is decomposed into a stationary part and a non-stationary part described by a finite basis. For example, $\log \kappa : D \rightarrow \mathbb{R}$ is split into a stationary contribution $\log \kappa_0$ and a spatially-varying $\log \kappa_{\text{NS}} : D \rightarrow \mathbb{R}$, giving $\log \kappa(s) = \log \kappa_0 + \log \kappa_{\text{NS}}(s)$ for $s \in D$. Here, $\int_D \log \kappa_{\text{NS}}(s) ds = 0$ so that it is orthogonal from the constant part.

3.1. Parametrization and prior for stationarity

Instead of placing priors directly on κ_0 , $v_{x,0}$ and $v_{y,0}$, we define them through the stationary parts ρ_0 , a_0 and ψ_0 of the interpretable parameters. The prior for the angle ψ_0 is set to the uniform distribution $\psi_0 \sim \text{Unif}(-\pi/2, \pi/2)$, meaning we do not favor some directions more than others. For range and marginal standard deviation, we follow Fuglstad et al. (2019), and specify a joint PC prior for (ρ_0, σ_0) as

$$\pi(\rho, \sigma) = \lambda_\rho \lambda_\sigma \exp\{-\lambda_\rho \rho^{-1} - \lambda_\sigma \sigma\}, \quad \rho, \sigma > 0, \quad \lambda_\rho, \lambda_\sigma > 0, \quad (8)$$

where λ_ρ and λ_σ are hyperparameters selected so that C_ρ is the prior median for range and C_σ is the prior median for marginal variance.

For selecting $\pi(a)$, we view the anisotropic model as a flexible extension of an isotropic base model. Let $\mathbf{v} \sim \mathcal{N}(\mathbf{0}, \sigma_\mathbf{v}^2 \mathbf{I})$, with the hyperparameter $\sigma_\mathbf{v} > 0$ controlling the marginal standard deviation. As the variance approaches zero, the anisotropy approaches $a = 1$. Since $(v_x^2 + v_y^2)/\sigma_\mathbf{v}^2$ is chi-square distributed with 2 degrees of freedom, the CDF of $a = \exp(\|\mathbf{v}\|)$ is

$$P(a \leq k) = P\left(\frac{v_x^2 + v_y^2}{\sigma_\mathbf{v}^2} \leq \left(\frac{\log k}{\sigma_\mathbf{v}}\right)^2\right) = 1 - \exp\left\{-\frac{1}{2}\left(\frac{\log k}{\sigma_\mathbf{v}}\right)^2\right\}, \quad (9)$$

which we differentiate it to obtain

$$\pi(a) = \sigma_\mathbf{v}^{-2} \frac{\log a}{a} \exp\left\{-\frac{1}{2}\left(\frac{\log a}{\sigma_\mathbf{v}}\right)^2\right\}, \quad a \geq 1.$$

Instead of having to specify $\sigma_\mathbf{v}$ directly, we control the prior with a hyperparameter C_a chosen so that $P(a > C_a) = 0.05$.

Lastly, inspired by the rSPDE package (Bolin and Simas, 2023), $\pi(v)$ is set to a beta distribution constructed on the user-specified interval $(0, v_{\max})$. The prior density becomes

$$\pi(v) = \frac{v_{\max}}{B(p, q)} \left(\frac{v}{v_{\max}}\right)^{p-1} \left(1 - \frac{v}{v_{\max}}\right)^{q-1}, \quad 0 < v < v_{\max}, \quad p, q > 0, \quad (10)$$

where $B(p, q)$ denotes the beta function. To simplify prior specification by avoiding having to select p and q directly, we reparameterize the beta distribution using its mean value C_v and the length $C_{v, \text{HPD}}$ of the 95% highest posterior density (HPD) interval. This length is defined as the width of the interval $\{v : \pi(v) \geq k\}$ where

$$\int_{\{v : \pi(v) \geq k\}} \pi(v) dv = 95\%.$$

A shorter interval implies a more concentrated and informative prior, while a longer interval results in a less informative one.

3.2. Parametrization and prior for non-stationarity

The parameterization of the non-stationarity is the same for all four functions, so we use $\log \kappa_{\text{NS}}(\cdot)$ for demonstration. We follow Fuglstad et al. (2015b) and impose a GRF on $\log \kappa_{\text{NS}}(\cdot)$ by solving

$$\begin{cases} -\Delta \log \kappa_{\text{NS}}(s) = \mathcal{W}_\kappa(s)/\sqrt{\tau_\kappa}, & s \in \mathcal{D}, \\ \nabla \log \kappa_{\text{NS}}(s) \cdot \mathbf{n}(s) = 0, & s \in \partial \mathcal{D}, \end{cases} \quad (11)$$

where $\mathcal{W}_\kappa(\cdot)$ is Gaussian white noise and $\tau_\kappa > 0$ is a penalty parameter. This motivates us to write

$$\log \kappa(s) \approx \log \kappa_0 + \sum_{(k,l) \in E} \alpha_{kl} f_{kl}(s), \quad s \in \mathcal{D}, \quad (12)$$

where $E = (\{0, 1, \dots, M\} \times \{0, 1, \dots, N\}) \setminus \{(0, 0)\}$, and $f_{kl}(\cdot)$ are eigenfunctions of $-\Delta$ on \mathcal{D} with zero Neumann boundary conditions. We use the normalized eigenfunctions

$$f_{kl}(x, y) = \frac{1}{C_{kl}\sqrt{AB}} \cos\left(\frac{k\pi(x - A_1)}{A}\right) \cos\left(\frac{l\pi(y - B_1)}{B}\right), \quad s \in \mathcal{D}, \quad (k, l) \in E \quad (13)$$

where $A = A_2 - A_1$, $B = B_2 - B_1$. $C_{kl} = 2$ if k and l are both non-zero, and $C_{kl} = \sqrt{2}$ of exactly one of k and l are non-zero.

Let $\boldsymbol{\alpha}_\kappa = (\alpha_{\kappa,kl})_{(k,l) \in E}^T$ be the vector of coefficients, then a truncated spectral representation of the SPDE from Equation (11) gives rise to the discretized SPDE

$$-\Delta \left(\log \kappa_0 + \sum_{(k,l) \in E} \alpha_{\kappa,kl} f_{kl}(s) \right) = \frac{1}{\sqrt{\tau_\kappa}} \sum_{(k,l) \in E} z_{kl} f_{kl}(s), \quad z_{kl} \stackrel{\text{iid}}{\sim} \mathcal{N}(0, 1), \quad (k, l) \in E,$$

where the right-hand side follows from expanding the Gaussian white noise $\mathcal{W}_\kappa(\cdot)$ in terms of the basis functions. Due to linearity and orthogonality, we can solve for each coefficient separately, giving

$$\alpha_{\kappa,kl} \left[\left(\frac{\pi k}{A} \right)^2 + \left(\frac{\pi l}{B} \right)^2 \right] f_{kl}(s) = \frac{z_{kl}}{\sqrt{\tau_\kappa}} f_{kl}(s), \quad (k, l) \in E.$$

Thus, the coefficient vector $\boldsymbol{\alpha}_\kappa$ contains $(M + 1)(N + 1) - 1$ elements, and has distribution $\boldsymbol{\alpha}_\kappa \sim \mathcal{N}(\mathbf{0}, \tau_\kappa^{-1} \mathbf{Q}_{\text{NS}}^{-1})$. \mathbf{Q}_{NS} is a diagonal precision matrix with $Q_{\text{NS},i,i} = [(\pi k_i/A)^2 + (\pi l_i/B)^2]^{1/2}$ for $i = 1, \dots, (M + 1)(N + 1) - 1$, where k_i and l_i is the index pair corresponding to the ordering used for $\boldsymbol{\alpha}_\kappa$.

In the same way, $\log \sigma(\cdot)$, $v_x(\cdot)$ and $v_y(\cdot)$ respectively gives rise to $\boldsymbol{\alpha}_\sigma$, $\boldsymbol{\alpha}_{v_x}$ and $\boldsymbol{\alpha}_{v_y}$ with the corresponding distribution having penalty parameters τ_σ , τ_{v_x} and τ_{v_y} . When specifying the priors, we have to select coefficients $\boldsymbol{\tau} = (\tau_\kappa, \tau_\sigma, \tau_{v_x}, \tau_{v_y})^T$ which determines how much the non-stationarity is penalized. The non-stationarity can be controlled by setting a bound limiting the variability (Fuglstad et al., 2019, Appendix G.2). Using the interpretable parameter $\rho(\cdot)$ with stationary component ρ_0 , we choose the penalty τ_κ such that

$$P\left(\max_{s \in \mathcal{D}} \left| \log \left(\frac{\rho(s)}{\rho_0} \right) \right| > \log C_{\text{NS},\rho}\right) = 0.05. \quad (14)$$

Here, $C_{\text{NS},\rho} > 0$ is a user-defined threshold determining the upper bound. The probability in Equation (14) can be approximated using the known distribution of $\boldsymbol{\alpha}_\kappa$. Constructing a regular grid over the domain, we obtain a set of M spatial locations at which the ratio is evaluated. Then the probability is approximated as

$$P\left(\max_{s \in \mathcal{D}} \left| \log \left(\frac{\rho(s)}{\rho_0} \right) \right| > C_{\text{NS},\rho}\right) \approx \frac{1}{M} \sum_{i=1}^M \mathbb{1}\left(\max_{s \in \mathcal{S}} \left| \log \left(\frac{\rho(s)}{\rho_0} \right) \right| > \log C_{\text{NS},\rho}\right),$$

where $\mathbb{1}(\cdot)$ is the indicator function. By repeating this process for different τ_κ , we select the value that yields an estimated probability close to the desired value 0.05. The penalties for the remaining non-stationary parameters are set though a similar procedure, where we specify thresholds limiting the ratio between the parameter and its stationary component. We assume $\tau_{v_x} = \tau_{v_y}$ for the $v_x(\cdot)$ and $v_y(\cdot)$, meaning we only choose $C_{\text{NS},v}$.

For ease of notation, we construct a vector of stationary parameters $\boldsymbol{\theta}_S = (\kappa_0, \sigma_0, v_{x,0}, v_{y,0}, v)^T$, and $\boldsymbol{\theta}_{\text{NS}} = (\boldsymbol{\alpha}_\kappa^T, \boldsymbol{\alpha}_\sigma^T, \boldsymbol{\alpha}_{v_x}^T, \boldsymbol{\alpha}_{v_y}^T)^T$ with coefficients controlling the non-stationary parameters. These vectors are used during optimization for parameter estimation. Summarizing the priors, the stationary $\boldsymbol{\theta}_S$ is controlled by hyperparameters C_ρ , C_σ , C_a , C_v , $C_{v,\text{HPD}}$ and v_{\max} , while the hyperparameters for the non-stationarity $\boldsymbol{\theta}_{\text{NS}}$ are $C_{\text{NS},\rho}$, $C_{\text{NS},\sigma}$ and $C_{\text{NS},v}$.

4. Spatial regression model

4.1. Hierarchical model

Assume we have a vector of n observations $\mathbf{y} = (y_1, \dots, y_n)^T$ made at locations $s_1, \dots, s_n \in \mathcal{D}$, respectively. For $i = 1, \dots, n$, the observations are independently modeled as

$$y_i | \eta(s_i), \sigma_N^2 \sim \mathcal{N}(\eta(s_i), \sigma_N^2),$$

where $\eta(\cdot)$ is a spatially varying true signal. It is modeled as the GRF

$$\eta(\cdot) = \mathbf{x}(\cdot)^T \boldsymbol{\beta} + u(s), \quad s \in \mathcal{D},$$

where $\mathbf{x}(\cdot)$ is a spatially-varying vector of p covariates, $\boldsymbol{\beta}$ are the p coefficients, and $u(\cdot)$ is the GRF from Section 2.1. For computations, we replace $u(\cdot)$ by the approximation $\tilde{u}(\cdot)$ described in Section 2.2. This gives the vector representation

$$\mathbf{y} = \mathbf{X}\boldsymbol{\beta} + \mathbf{A}\mathbf{P}_R\tilde{\mathbf{w}} + \boldsymbol{\epsilon},$$

where \mathbf{X} is the $n \times p$ design matrix, \mathbf{A} is the $n \times m$ matrix mapping from location to basis functions, $\tilde{\mathbf{w}} \sim \mathcal{N}(0, \tilde{\mathbf{Q}}^{-1})$ as described in Section 2.2, and $\boldsymbol{\epsilon} | \sigma_N^2 \sim \mathcal{N}(\mathbf{0}, \sigma_N^2 \mathbf{I})$. The covariance model is described by parameters $\boldsymbol{\theta} = (\boldsymbol{\theta}_S^T, \boldsymbol{\theta}_{NS}^T)^T$ that control ν , $\log \kappa(\cdot)$, $\log \sigma(\cdot)$, $v_x(\cdot)$, $v_y(\cdot)$ as discussed in Section 3, and we can write the hierarchical model

$$\begin{aligned} \mathbf{y} | \boldsymbol{\beta}, \tilde{\mathbf{w}}, \sigma_N^2 &\sim \mathcal{N}(\mathbf{X}\boldsymbol{\beta} + \mathbf{A}\mathbf{P}_R\tilde{\mathbf{w}}, \sigma_N^2 \mathbf{I}), \\ \boldsymbol{\beta} &\sim \mathcal{N}(\mathbf{0}, \mathbf{I}/\tau_\beta), \tilde{\mathbf{w}} | \boldsymbol{\theta} \sim \mathcal{N}\left(\mathbf{0}, \tilde{\mathbf{Q}}^{-1}(\boldsymbol{\theta})\right), \\ \sigma_N^2 &\sim \pi(\sigma_N^2), \boldsymbol{\theta} \sim \pi(\boldsymbol{\theta}). \end{aligned}$$

$\pi(\sigma_N^2)$ is given the PC prior from Simpson et al. (2017) with the median C_{σ_N} as hyperparameter, and τ_β is a small value corresponding to a vague prior on the coefficients. Additionally we have the hyperparameters described in Sections 3.1 and 3.2 for the covariance model.

4.2. Parameter estimation and prediction

Collecting the vectors controlling the spatial and fixed effects in $\mathbf{z} = (\tilde{\mathbf{w}}^T, \boldsymbol{\beta}^T)^T$, define the matrices

$$\mathbf{S} = [\mathbf{A}\mathbf{P}_r \quad \mathbf{X}] \quad \text{and} \quad \mathbf{Q}_z = \begin{bmatrix} \mathbf{Q} & \mathbf{0} \\ \mathbf{0} & \tau_\beta \mathbf{I} \end{bmatrix}.$$

Then we can write the hierarchical model as

$$\begin{aligned} \mathbf{y} | \mathbf{z}, \boldsymbol{\theta}, \sigma_N^2 &\sim \mathcal{N}(\mathbf{S}\mathbf{z}, \sigma_N^2 \mathbf{I}) \\ \mathbf{z} | \boldsymbol{\theta} &\sim \mathcal{N}(\mathbf{0}, \mathbf{Q}_z^{-1}). \end{aligned}$$

Denote the posterior distribution as $\pi(\boldsymbol{\theta} | \mathbf{y})$, then the procedure described in Fuglstad et al. (2015b, Appendix C) gives

$$\begin{aligned} \log \pi(\boldsymbol{\theta}, \sigma_N^2 | \mathbf{y}) &\propto \log \pi(\sigma_N^2) + \log \pi(\boldsymbol{\theta}_S) + \log \pi(\boldsymbol{\theta}_{NS}) \\ &\quad + \frac{1}{2} \log |\mathbf{Q}_z| - \frac{n}{2} \log \sigma_N^2 - \frac{1}{2} \log |\mathbf{Q}_C| \\ &\quad - \frac{1}{2} \boldsymbol{\mu}_C^T \mathbf{Q}_z \boldsymbol{\mu}_C - \frac{1}{2} \sigma_N^{-2} (\mathbf{y} - \mathbf{S}\boldsymbol{\mu}_C)^T (\mathbf{y} - \mathbf{S}\boldsymbol{\mu}_C), \end{aligned} \tag{15}$$

where $\mathbf{Q}_C = \mathbf{Q}_z + \mathbf{S}^T \mathbf{S} / \sigma_N^2$ and $\boldsymbol{\mu}_C = \mathbf{Q}_C^{-1} \mathbf{S}^T \mathbf{y} / \sigma_N^2$. Here $\boldsymbol{\mu}_C$ and \mathbf{Q}_C are the mean vector and precision matrix for $\mathbf{z} | \mathbf{y}, \sigma_N^2, \boldsymbol{\theta}$. The MAP $(\hat{\boldsymbol{\theta}}^T, \hat{\sigma}_N^2)^T$ of $(\boldsymbol{\theta}^T, \sigma_N^2)^T$ are the parameters maximizing this log-likelihood.

For a new set of k unobserved locations $s_1^*, \dots, s_k^* \in \mathcal{D}$, the posterior mean and marginal variance of $\eta(\cdot)$ can be predicted at the unobserved locations using the density of $\mathbf{z}|\mathbf{y}, \hat{\theta}, \hat{\sigma}_N^2$. Define the matrix $\mathbf{S}_P = [\mathbf{A}_P \mathbf{P}_R \quad \mathbf{X}_P]$, where \mathbf{X}_P is the $k \times p$ dimensional design matrix for the prediction locations, and \mathbf{A}_P is the $k \times m$ dimensional matrix mapping the triangulation to the prediction locations. Let $\boldsymbol{\eta}^* = (\eta(s_1^*), \dots, \eta(s_k^*))^T$, then

$$\boldsymbol{\eta}^* | \mathbf{y}, \hat{\theta}, \hat{\sigma}_N^2 \sim \mathcal{N}(\mathbf{S}_P \boldsymbol{\mu}_C, \mathbf{S}_P \mathbf{Q}_C^{-1} \mathbf{S}_P^T),$$

where we only need to compute the diagonal of $\mathbf{S}_P \mathbf{Q}_C^{-1} \mathbf{S}_P^T$ for marginal properties. To predict a new observation, we also need to add independent Gaussian measurements errors with variance $\hat{\sigma}_N^2$, and compute the diagonal of $\mathbf{S}_P \mathbf{Q}_C^{-1} \mathbf{S}_P^T + \hat{\sigma}_N^2 \mathbf{I}$ to find the prediction variances.

4.3. Optimization strategy

Gradient information is required for reliable convergence when estimating the model parameters. Fuglstad et al. (2015b, Appendix D) derive analytical gradients for a related non-stationary model with $\nu = 1$, but extending these derivations to fractional models is considerably more involved due to the rational approximation. The rSPDE package (Bolin and Simas, 2023) instead relies on numerical differentiation. However, this does not scale well as the number of parameters increases. As an alternative, we compute gradients of the log-likelihood using AD. AD evaluates derivatives through a process called *backpropagation*, which involves systematically applying the chain rule to the sequence of operations defining the log-likelihood. This can be computed efficiently even in high-dimensional parameter spaces, and yields gradients that are exact up to machine precision.

A challenge when using AD is differentiating the sparse matrix operations required for our likelihood evaluation. Even if an operation uses a sparse matrix, most AD frameworks do not encode sparsity patterns and instead treat the matrices as dense during backpropagation. Modern frameworks such as PyTorch (Paszke et al., 2019) provide partial support for sparse tensors, sparse matrix addition and multiplication are still differentiated as if they were dense. There is no native way of computing log-determinants or solving linear systems using sparse matrices. This removes the computational benefits of the SPDE approach. To address this, we implement custom PyTorch functions by adopting the masking strategy proposed by Nytko et al. (2023), which assumes that gradient matrices share the same sparsity pattern as their corresponding inputs. This preserves sparsity throughout the differentiation process and additionally allows us to exploit the *partial inverse* (Takahashi, 1973; Rue and Martino, 2007) when differentiating sparse log-determinants. Details are provided in Appendix A.

When applying AD to the rational approximation, we must also specify how to differentiate with respect to the smoothness parameter ν . The rational approximation depends on $k_\beta = \max\{1, \lfloor \beta \rfloor\}$ and whether ν is integer valued, which implies that the computational structure of the log-likelihood changes at $\nu \in \mathbb{N}$. As a result, the log-likelihood is not differentiable with respect to ν at these points. However, in practice this is rarely an issue, as the optimizer almost never proposes exactly integer values of ν . Moreover, since $k_\beta = 1$ for all $\nu \in (0, 3)$, the computational graph remains unchanged within this interval. To apply the AD-approach to our model, we therefore assume $\nu \in (0, 3) \setminus \mathbb{N}$.

We use the Adam optimizer (Kingma and Ba, 2017) for parameter estimation. To limit computation time, we impose a stopping criterion based on the relative change in the log-likelihood. The optimization is terminated when the absolute change in the log-likelihood between successive iterations is less than 10^{-4} times its current value.

5. Simulation study

5.1. Data-generating models

To assess the importance of non-stationarity and fractional smoothness in prediction, we study the parameter estimation and predictive performance of the proposed model. We use data generated from a stationary and a non-stationary model, both with the same smoothness parameter $\nu = 0.5$. In the stationary model, $\kappa(\cdot)$, $\sigma(\cdot)$, $v_x(\cdot)$, and $v_y(\cdot)$ are constant over

the domain. In the non-stationary model, $\kappa(\cdot) \equiv \kappa_0$ and $\sigma(\cdot) \equiv \sigma_0$ remain constant, while the anisotropy components $v_x(\cdot)$ and $v_y(\cdot)$ vary spatially and are each represented using eight basis functions.

We use the SPDE approach to generate data from a centered GRF on the domain $\mathcal{D} = [0, 20] \times [0, 20]$. To reduce boundary effects, we embed \mathcal{D} in an extended domain obtained by adding 20 units on each side. We construct the finite-element discretization using fmesher (Lindgren, 2024), resulting in a triangular mesh with 10 441 vertices and 20 778 elements. For the rational approximation, we use order $k = 1$. Figure 2 shows a realization from the non-stationary field, which is nearly isotropic in the center but becomes increasingly anisotropic near the boundary. As a consequence, even though $\sigma(\cdot)$ is stationary in the model specification, Figure 2b shows that the marginal standard deviation also varies slightly over the domain.

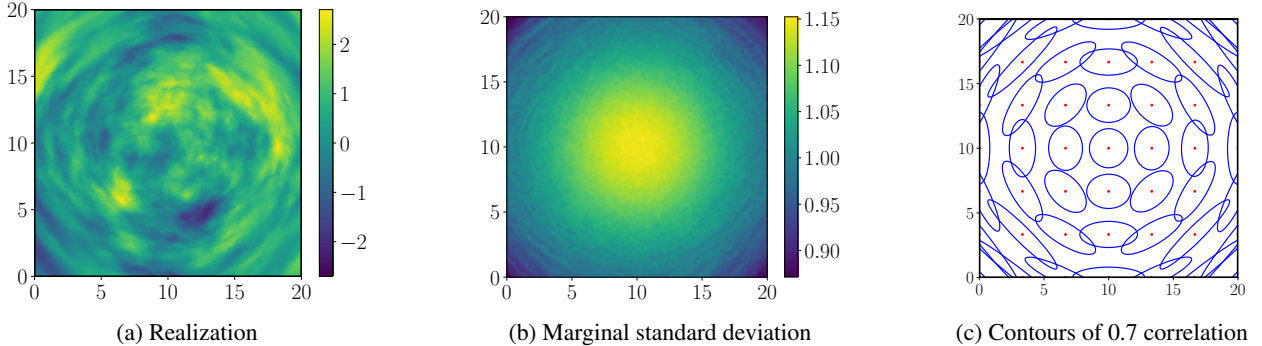


Figure 2: Visualizations of the non-stationary SPDE model with $v = 0.5$. Used for generating evaluation data in the simulation study.

5.2. Candidate models

We compare four classes of candidate models. All are based on the hierarchical specification from Section 4, but where the fixed effects are omitted. The first class is a non-fractional and stationary model (NF-S), which assumes fixed smoothness $v = 1$ and stationary parameters. The second class is a non-fractional and non-stationary model (NF-NS), which allows $\kappa(\cdot)$, $\sigma(\cdot)$, $v_x(\cdot)$, and $v_y(\cdot)$ to vary spatially. We also consider a fractional and stationary model (F-S), and our proposed fractional and non-stationary model (F-NS). Here the smoothness v is estimated using observations. Each model is discretized using the same mesh as in the data-generating step, and the fractional models employ an order $k = 1$ rational approximation.

For parameter estimation, stationary parameters are initialized at random values within $\pm 50\%$ of the true value, while the coefficients governing non-stationarity are initialized to zero. The hyperparameters C_ρ , C_σ and C_{σ_N} for the prior medians are set to the true value, while we let $C_a = 4$. When estimating smoothness, the prior for v is specified with $C_v = 1.0$, $C_{v,HPD} = 1.8$ and $v_{\max} = 2.0$. For the non-stationary models, we consider both 8 or 16 basis functions per non-stationary parameter. To reduce the number of candidates, all parameters use the same amount of basis functions. Every non-stationary parameter is also assumed to use the same hyperparameter C_{NS} for controlling the flexibility, where we consider $C_{NS} \in \{2, 5, 10\}$, corresponding to strict, moderate and small penalization. For ease of notation, we denote a model with 8 basis functions and a $C_{NS} = 2$ as B8-C2, and introduce similar abbreviations for the other combinations.

5.3. Evaluation

For the evaluation, we generate 25 independent datasets from each data-generating model. For each dataset, we sample 1000 locations $s_{i,1}, \dots, s_{i,1000}$ uniformly from the interior of the spatial domain and interpolate the latent field at these locations. Observation error is added as Gaussian noise with marginal variance $\sigma_N^2 = 0.1$, yielding observations $y_{i,1}, \dots, y_{i,1000}$. To investigate the effect of data density, we fit each candidate model using subsets of the 1000 observed

locations with size 125, 500 and 1000. For each subset size, parameter bias is evaluated by averaging the parameter estimates over the 25 simulated datasets. Predictions are made on a regular 100×100 grid covering D . For each simulation and each subset size, the estimated parameters are used to compute the posterior distribution of the latent field at all prediction locations. Interpolating the values of the true latent field at the prediction locations, we compare them to the predicted posterior means and standard deviations by computing the average RMSE and CRPS across the 25 simulations.

5.4. Impact of basis functions and penalties

We begin by examining how model performance depends on the number of basis functions and the choice of penalty parameters. To isolate these effects, we focus on the stationary F-S model and the different parameterizations of the non-stationary F-NS model. All models use a fixed smoothness parameter $v = 0.5$. Recall that the true non-stationary data were generated by an F-NS model with 8 basis functions. Models using 8 or 16 basis functions should therefore in principle be capable of representing the spatial variation of the data-generating model.

Fitting the models to observations from the non-stationary data-generating model, Figure 3 shows RMSE and CRPS as functions of the number of observations. With only 125 observations, the more flexible models perform slightly worse than the simpler ones. When at least 500 observations are available, the flexible models outperform the simpler alternatives. This indicates that increased flexibility allows the model to capture non-stationarity when sufficient data are available, but leads to overfitting when the sample size is small.

Comparing the models with 8 and 16 basis functions, we find that the B16-C10 model is unstable and occasionally produces substantially worse predictions than the other models. Notably, these poor predictions occur both for small sample sizes and when using all 1000 observations. In contrast, B16-C5 performs similarly to B8-C10 for 500 and 1000 observations, and slightly better for 125 observations. This shows that using a larger number of basis functions is not inherently problematic, provided that a stronger penalty is applied.

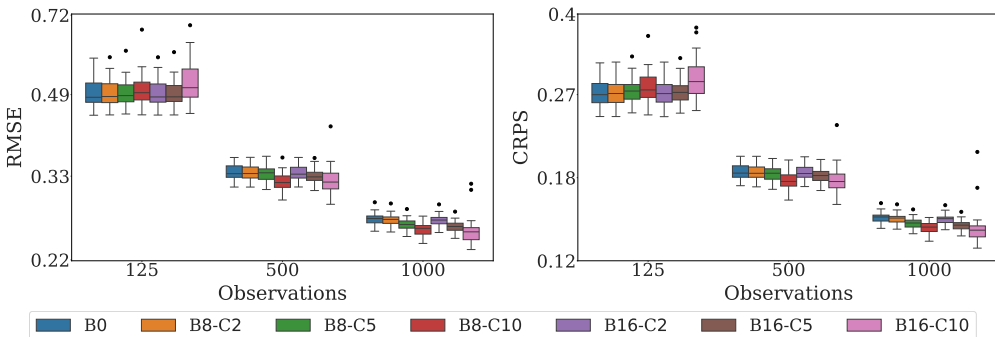


Figure 3: Log-scaled RMSE and CRPS scores for data generated by a non-stationary model with smoothness $v = 0.5$. Plotted as functions of the number of observations.

5.5. Estimating the smoothness

To assess the effect of estimating the smoothness parameter, we no longer fix $v = 0.5$. Instead, we estimate v using the AD approach and compare the fractional models F-S and F-NS to their non-fractional counterparts NF-S and NF-NS. For the non-stationary models F-NS and NF-NS, we use 8 basis functions and set $C_{NS} = 10$, which was found to provide the best performance when at least 500 observations are available.

Fitting to observations from the stationary data-generating model, Figure 4 shows predictive RMSE and CRPS as functions of the number of observations. For 125 observations, the stationary models outperform the non-stationary ones, while performance is comparable for 500 and 1000 observations. Fractional models perform slightly better than non-fractional models across all sample sizes, but the differences are small. Table 1 in Appendix B shows parameter

estimates based on 500 observations. Both F-S and F-NS estimate the smoothness parameter with relatively small bias. This suggests that even when smoothness is estimated accurately, the resulting gains in predictive performance are limited in this setting.

We next fit the candidate models to data generated from the non-stationary process. Parameter estimates from Table 2 in Appendix B show that the fractional models again estimate the smoothness parameter with low bias. Predictive RMSE and CRPS are shown in Figure 5. As in the stationary case, differences between fractional and non-fractional models are modest. In contrast, the non-stationary models consistently outperform the stationary models when at least 500 observations are available, highlighting the importance of modeling non-stationarity when sufficient data is present.

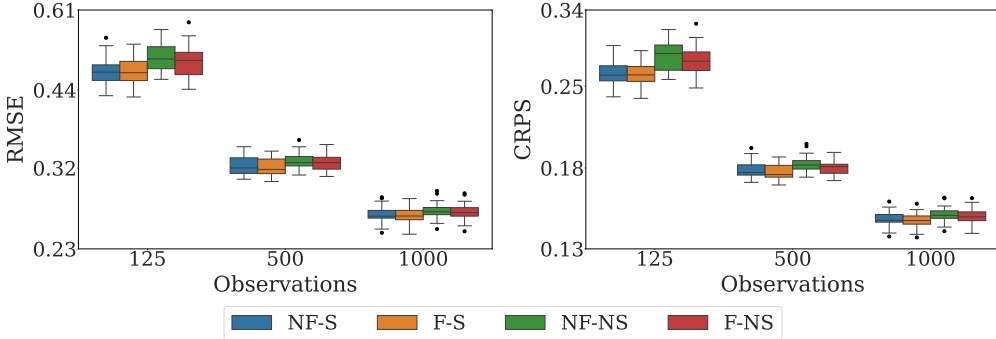


Figure 4: Log-scaled RMSE and CRPS scores for data generated by a stationary model with smoothness $\nu = 0.5$. Plotted as functions of the number of observations.

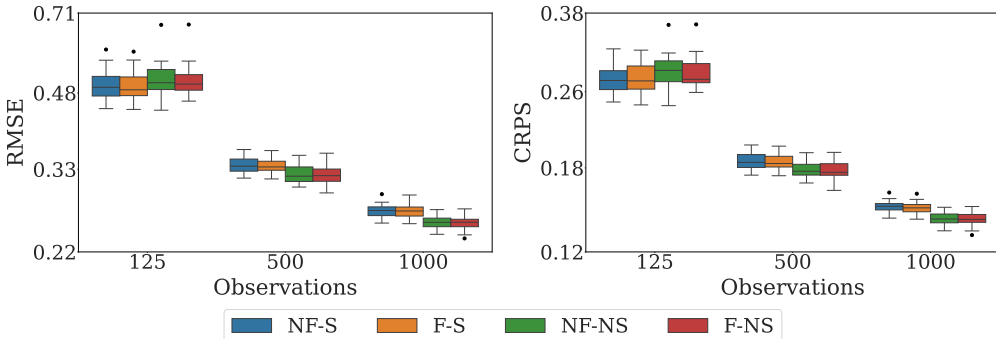


Figure 5: Log-scaled RMSE and CRPS scores for data generated by a non-stationary model with smoothness $\nu = 0.5$. Plotted as functions of the number of observations.

6. Case-studies

We evaluate the added value of the spatial regression model through two case studies.

6.1. Ocean salinity

The first is a dataset consisting of salinity values in Trondheimsfjorden, and comes from the SINMOD model developed by SINTEF Ocean (SINTEF, 1987; Slagstad and McClimans, 2005). This is a numerical ocean model that simulates ocean dynamics based on atmospheric forces, freshwater input and tides (Berild and Fuglstad, 2023). SINMOD reports the salinity in *practical salinity units* (psu), which describe the grams of salt per kilogram of seawater (Talley, 2011). The data is provided on a grid with a spatial resolution of 32 m, using a polar stereographic projection centered on the North Pole. For this analysis, the coordinates are transformed to the *Universal Transverse Mercator* (UTM) zone

32V projection. We examine the hourly salinity on the 2nd of May 2020, simulated at 4196 locations and at a depth of 0.5 m. The collections of data are treated as 24 independent spatial realizations, and we center them by subtracting the location-wise mean across realizations. To replicate measurement error, we add Gaussian noise with a marginal standard deviation of $\sigma_N = 0.1$ psu. This corresponds to a signal-to-noise ratio of approximately 1%. Figure 6 shows a realization of the centered salinity anomalies, with a satellite image of the region placed underneath for reference. Observe a notable spatial variation near the mouth of the Nidelva River, where freshwater mixes with the salty seawater.

We continue using the same four model classes as in the simulation study. Based on the results of the simulation study, we found that using 8 basis functions and $C_{NS} = 10$ performed well for the non-stationary models, and we therefore adopt this configuration for the analysis. To guide the choice of priors, we first perform a preliminary analysis of the full dataset using a NF-S model with diffuse priors. We estimate $\hat{\rho}_0 = 1.2$ km and $\hat{\sigma}_0 = 1$ psu, and use these to set the hyperparameters C_ρ and C_σ . From the added noise we set $C_{\sigma_N} = 0.1$, and use $C_a = 4$ for the anisotropy. We have little prior knowledge about the smoothness of the data, as previous analyses have used a fixed $\nu = 1$ (Lilleborge, 2021; Berild and Fuglstad, 2023, 2024). Therefore, we choose the weakly informative $C_\nu = 1.0$, $C_{\nu,HPD} = 1.8$ and $\nu_{\max} = 2.0$. Discretizing the models, the domain is first expanded by 2.4 km on all sides to reduce boundary effects, and we use fmesher to construct a triangulation with 10654 vertices and 21143 elements.

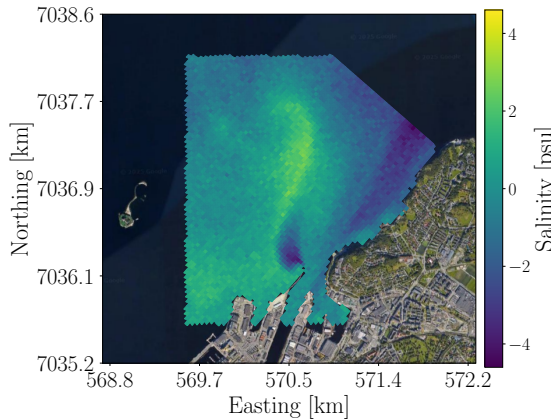


Figure 6: Satellite image of Ladehammeren overlaid with centered salinity anomalies from the salinity dataset. Illustrating the relationship between simulated data and the underlying physical processes.

First, we examine whether the non-stationary models can capture any non-stationary behavior that aligns with known physical processes in the domain. Fitting the F-NS model to the full dataset, Figure 7 shows the estimated iso-correlation curves and marginal standard deviation. At the bottom of the domain, in the area near where Nidelva flows into the fjord, the model estimates a low correlation range and high marginal standard deviation. This could be explained by the mixing of freshwater and saltwater, which increases variability and reduces the spatial range compared to areas further out in the fjord. Moreover, the estimated anisotropy indicates stronger correlation along the outflow direction, consistent with the movement of the water.

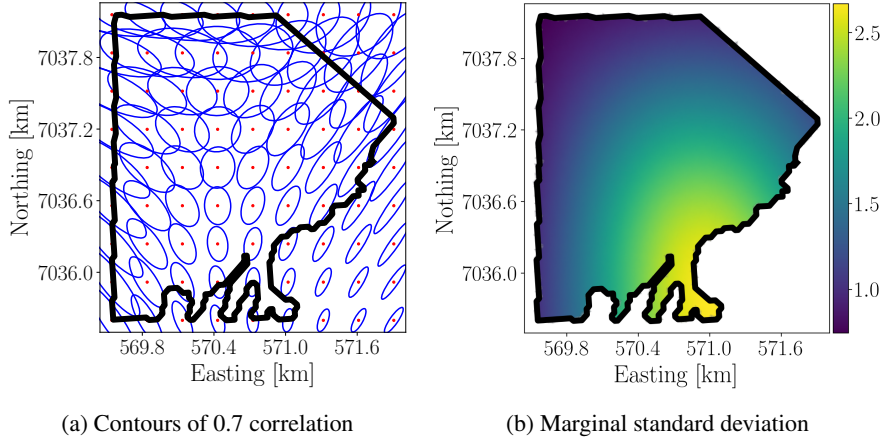


Figure 7: Estimates of non-stationary properties when fitting F-NS to all available salinity data.

Next, we evaluate the predictive performance of the models, which requires specifying training and test datasets. Because the data are observed on a dense spatial grid, randomly selecting training and test locations across the domain would place many test locations close to observed ones, causing the evaluation to be dominated by short-range interpolation and observation noise. Instead, we adopt an evaluation strategy in which one realization is held out at a time, and model parameters are estimated using observations from all locations in the remaining realizations. Predictions are then made for the held-out realization, conditioning on observations at only a randomly selected subset of locations, with the number of observed locations varied between 10 and 250. Predictive accuracy at the unobserved locations is assessed using RMSE and CRPS. This procedure is repeated for each of the 24 realizations, allowing us to compute empirical means and standard deviations of the scores. Although this setup is less common in practice, it arises in several real-world applications, such as the autonomous underwater vehicle studies Lilleborge (2021); Berild and Fuglstad (2023, 2024).

Figure 8 shows RMSE and CRPS as functions of the number of observations in the held-out realization. The non-stationary models consistently outperform the stationary ones, with the largest differences for 50 observations. For 250 observations, the performance gap narrows as most test locations lie close to observed ones. In contrast, fractional and non-fractional models show similar predictive accuracy. From Table 3 in Appendix B, the estimated fractional smoothness parameters are 0.92 and 0.88 for F-S and F-NS, respectively. These values are close to one, suggesting near non-fractional behavior.

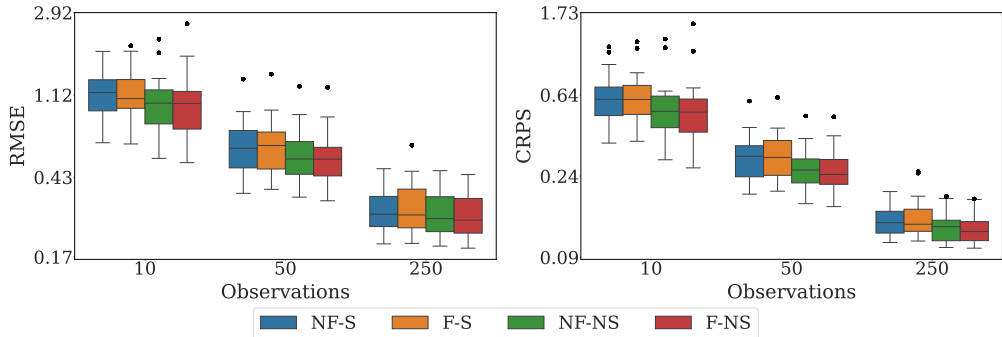


Figure 8: Log-scaled RMSE and CRPS scores for the evaluation using the salinity dataset. Results plotted as functions of the number of observations.

6.2. Precipitation data

The second dataset contains climate reanalysis data describing average summer precipitation over the conterminous U.S. Climate reanalysis combines a climate model with observations to reconstruct past climate patterns (C3S, 2025). This dataset was generated by the Experimental Climate Prediction Center Regional Spectral Model as part of the North American Regional Climate Change Assessment Program. It covers a 26-year period from 1979 to 2004, and includes average precipitation values measured in centimeters at 4112 locations given in geographic coordinates across the domain. We select this dataset because prior studies have indicated the presence of a fractional smoothness. In particular, Genton and Kleiber (2015) found that an exponential covariance model may be appropriate in parts of the domain, while Bolin and Kirchner (2020) estimated a smoothness parameter of $v = 0.44$.

To prepare the precipitation data for spatial modeling, a cube-root transformation is applied so that a Gaussian distribution can be assumed (Genton and Kleiber, 2015). Each realization of the transformed data is also centered by subtracting the mean over the realizations. Figure 9a shows the processed anomalies for 1979. The spatial correlation range appears shorter in the southwest and increases toward the east. The pattern is neither unique to this specific year, but shows up in most realizations. A possible explanation is the differences in altitude over the domain, as we see in Figure 9b that the Rocky Mountains lead to the western region being much more mountainous.

Specifying the stationary priors, we again perform a preliminary analysis using a NF-S model. The hyperparameters C_ρ , C_σ , and C_{σ_N} are set based on the estimated values $\hat{\rho}_0 = 5^\circ$, $\hat{\sigma}_0 = 0.1$ cm, and $\hat{\sigma}_N = 0.02$ cm, while C_a is set to 4. Choosing $\pi(v)$, we base the prior on previous studies and adopt a more informative specification than for the salinity data. Specifically, we let $C_v = 0.5$, $C_{v,HPD} = 0.8$, and $v_{\max} = 1.0$. Discretizing the model, we expand the domain by 20° on each side and triangulate it to obtain 9555 vertices and 18939 elements.

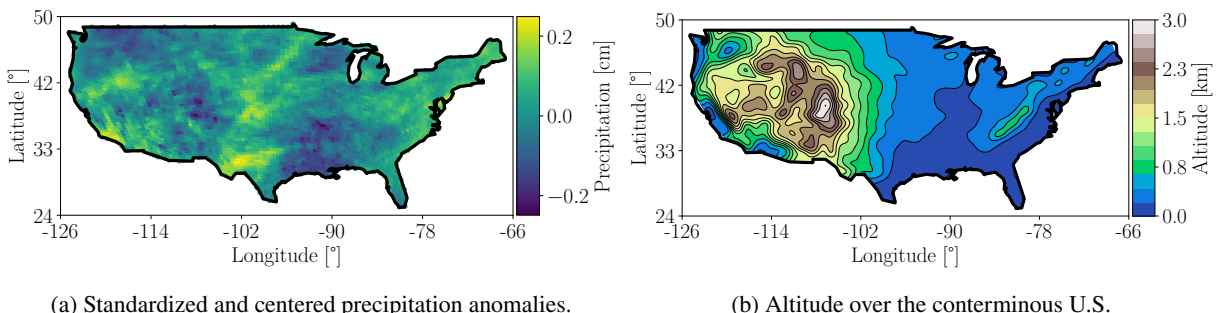


Figure 9: Precipitation anomalies and altitude over the spatial domain. Data is from the year 1979.

As for the salinity data, we begin our analysis by fitting the F-NS to all available data. The estimated iso-correlation curves and marginal standard deviation are shown in Figure 10. In the western part of the domain, the model estimates a shorter correlation range. In the east, a slight non-stationary anisotropic pattern emerges, with stronger correlation along the longitudinal axis. This may be a result of the Gulf Stream affecting the eastern climate. Figure 10b also shows a higher marginal standard deviation in the southwest. This could be due to the complex terrain of the Rocky Mountains or Sierra Nevada, which introduces localized weather phenomena.

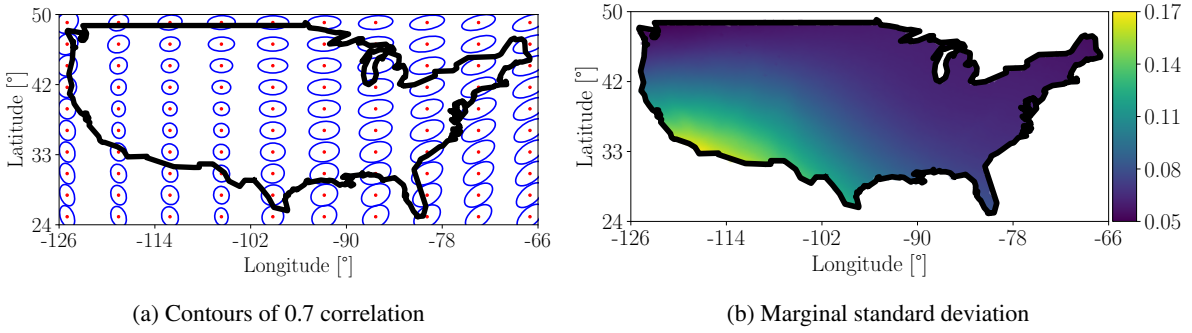


Figure 10: Estimates of non-stationary parameters when fitting F-NS to all available precipitation data.

Fitting the candidate models to the precipitation data by following the same procedure as for the salinity data, Figure 11 presents the RMSE and CRPS scores as functions of the number of observations. Unlike the salinity data, there is a clear difference between the fractional and non-fractional models. Here we see the fractional models consistently yield better predictions across all amounts of observations. Table 4 in Appendix B shows that the smoothness estimates for the fractional models are slightly below $v = 0.4$. These estimates are a bit lower than the $v = 0.44$ reported by Bolin and Kirchner (2020).

Another key difference from the salinity data is that the non-stationary models no longer outperform the stationary. This is surprising, as the differences in elevation led us to expect a difference in rainfall between the eastern and western regions. However, our findings align with those of Fuglstad et al. (2015b). When analyzing a similar dataset using a NF-NS model, they found that a stationary model performed approximately as well as the non-stationary. They argued that this was because the non-stationarity was incorporated into the wrong part of the model, and that it was the σ_N that had to be varied across the domain.

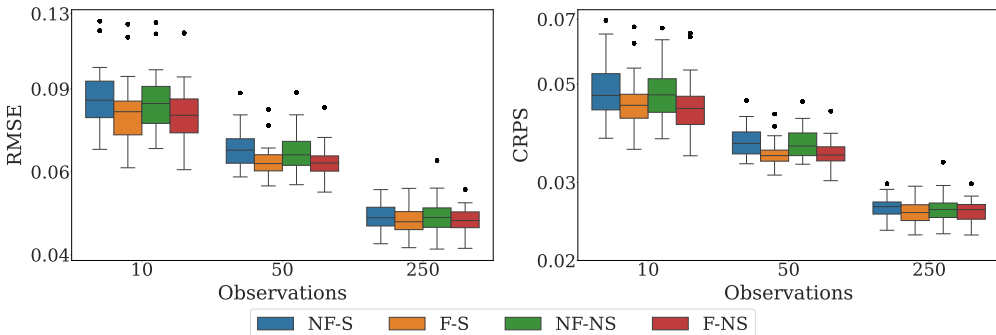


Figure 11: Log-scaled RMSE and CRPS scores for the evaluation using the precipitation dataset. Results plotted as functions of the number of observations.

7. Discussion

This paper extends the class of non-stationary SPDE models by combining non-stationary anisotropy with a fractional smoothness. Specifically, we combine the framework for non-stationary anisotropy developed by Fuglstad et al. (2015a,b), the parameterization of the diffusion matrix by Llamazares-Elias et al. (2024), and the rational approximation from Bolin and Kirchner (2020). The increased complexity comes with a higher risk of overfitting. To address this, we develop priors for the stationary and non-stationary components of the model. For the parameters specifying the stationary properties, we adopt the PC-like priors, while the non-stationary terms are controlled using

spline-based penalties from Fuglstad et al. (2015b). We also suggest an approach to setting these priors, and describe an interpretable approach for selecting penalties for the non-stationarity.

We further demonstrate the use of AD for parameter estimation in non-stationary fractional SPDEs. By combining AD with sparse matrix operations, we efficiently compute gradients without deriving analytical expressions or relying on numerical differentiation. This is particularly valuable for non-stationary models, where the number of parameters can be large. The approach relies on a masking strategy which introduces a small application error, but which preserves sparsity during backpropagation. Despite the current limitations in software support for sparse AD, the proposed methodology offers a practical and extensible framework for gradient-based inference in SPDE models with many parameters.

The simulation study demonstrates that the proposed model can reliably detect both fractional smoothness and non-stationarity when given a sufficient amount of data. With at least 500 observations from a single realization, the fractional models estimate the smoothness parameter with low bias, and the non-stationary models outperform their stationary counterparts when the data-generating process is non-stationary. With fewer observations, appropriate penalization becomes more important to avoid overfitting. The choice of penalty for the non-stationary components matters, as using more basis functions requires a stronger penalty to maintain stability. We also find that predictive improvements from estimating the fractional smoothness are modest, as non-fractional models can partially compensate by adjusting other parameters such as the correlation range.

The two case studies illustrate that the relative importance of fractional smoothness versus non-stationarity depends on the application. For the salinity data, non-stationary models clearly outperform stationary ones. The estimated non-stationary patterns also reflect known physical processes, such as shorter correlation ranges near the river mouth where freshwater mixes with seawater. However, the estimated smoothness was close to one, leading fractional and non-fractional models to perform similarly. For the precipitation data, the situation was reversed. Estimating the smoothness to around 0.4, we found the fractional models to outperform the non-fractional across all observation amounts. Yet, non-stationary models offer no improvement over stationary models. This is consistent with Fuglstad et al. (2015b), who for a similar dataset argued that non-stationarity may be more relevant in the measurement noise than in the spatial covariance. Together, these results show that the proposed model can help identify which type of flexibility is most relevant for a given dataset.

Based on our findings, we identify three key use cases for the proposed model. First, it serves as a tool for exploratory analysis, helping practitioners determine whether added complexity in the form of non-stationarity or fractional smoothness is needed. If the analysis reveals little evidence for such features, a simpler model can be used with greater confidence. Second, the model is valuable when the goal is to extract interpretable parameters that relate to underlying physical processes. Non-stationary anisotropy can reveal patterns such as water currents or terrain effects, while the estimated smoothness characterizes the local regularity of the field. Third, the model can improve predictive performance when there is reason to expect fractional or non-stationary behavior, as demonstrated by the case studies.

For future work, there are several promising directions. Continued development of AD-based estimation can further improve computational efficiency. The covariance-based rational SPDE approach by Bolin et al. (2024) offers improved numerical stability for larger values of ν , and adapting this to the non-stationary setting could extend the applicability of the model. Additionally, developing more principled strategies for penalizing non-stationary components remains an open problem. Progress on these fronts would make the proposed modeling framework even more practical for routine use.

A. Automatic differentiation of sparse matrices

Reverse-mode AD computes gradients by propagating derivatives backwards through a computational graph. For each operation in the graph, AD applies the chain rule via a *vector-Jacobian product* (VJP). Given a matrix operation $\mathbf{B} = f(\mathbf{A})$ that contributes to a scalar loss y , the VJP computes the *adjoint* $\bar{\mathbf{A}} = \partial y / \partial \mathbf{A}$ from the downstream adjoint

$\bar{\mathbf{B}} = \partial y / \partial \mathbf{B}$. By chaining these VJPs from output to input, AD obtains the gradient with respect to all parameters in a single backward pass. For a comprehensive introduction to AD, see Baydin et al. (2017).

For sparse matrices, standard AD frameworks often produce dense adjoints, which diminishes the computational benefits of the SPDE approach. This is not a limitation of AD itself, but occurs because most AD frameworks do not exploit known sparsity patterns, which are generally unavailable at runtime. Following Nytko et al. (2023), we address this by assuming the adjoint of a sparse matrix inherits its sparsity pattern. To formalize, define the *sparsity mask* of a matrix \mathbf{M} as

$$\text{mask}(\mathbf{M})_{ij} = \begin{cases} 1 & \text{if } \mathbf{M}_{ij} \neq 0, \\ 0 & \text{otherwise.} \end{cases}$$

We then enforce $\text{mask}(\bar{\mathbf{A}}) = \text{mask}(\mathbf{A})$ by element-wise multiplication $\bar{\mathbf{A}} \odot \text{mask}(\mathbf{A})$.

To implement custom sparse operations, we first derive the analytical VJPs and then apply the sparsity mask to obtain sparse adjoints. As examples, we consider solving a sparse linear system and computing the log-determinant, but the same approach applies to other sparse operations. Consider the linear system $\mathbf{AC} = \mathbf{B}$, where \mathbf{A} is a sparse matrix and \mathbf{B} is dense. Using differential calculus (Minka, 2000), the adjoints are

$$\bar{\mathbf{B}} = \mathbf{A}^{-T} \bar{\mathbf{C}} \quad \text{and} \quad \bar{\mathbf{A}} = -\bar{\mathbf{B}} \mathbf{C}^T.$$

The adjoint $\bar{\mathbf{B}}$ is computed by solving a transposed linear system. To preserve sparsity, we apply the mask to obtain

$$\bar{\mathbf{A}} = (-\bar{\mathbf{B}} \mathbf{C}^T) \odot \text{mask}(\mathbf{A}).$$

For the log-determinant $c = \log |\mathbf{A}|$ of a symmetric positive definite matrix \mathbf{A} , the adjoint without sparsity constraints is $\bar{\mathbf{A}} = \bar{c} \mathbf{A}^{-T}$ (Giles, 2008, Section 2.2). Applying the sparsity mask yields

$$\bar{\mathbf{A}} = (\bar{c} \mathbf{A}^{-T}) \odot \text{mask}(\mathbf{A}) = \bar{c} (\mathbf{A}^{-T} \odot \text{mask}(\mathbf{A})).$$

Notice that rather than computing the full inverse, we only need entries at the non-zero positions of \mathbf{A} . Using the sparse Cholesky factor, this partial inverse can be computed efficiently (Rue and Martino, 2007).

B. Parameter estimates from simulation study and case studies

B.1. Simulation study

Table 1

Average and empirical standard deviation of parameter estimates over 25 repeated simulations. The models are fitted using 500 observations from a single realization, generated by a stationary model with smoothness $\nu = 0.5$.

Model	Parameters					
	ν	ρ_0	a_0	ψ_0 [°]	σ_0	$\sigma_N [10^{-1}]$
True	0.5	10	1	–	1	3.2
NF-S	1.0	5.6 (1.2)	1.6 (0.2)	-5 (54)	0.9 (0.1)	3.4 (0.2)
NF-NS	1.0	6.8 (1.8)	1.6 (0.1)	6 (56)	0.9 (0.1)	3.3 (0.3)
F-S	0.5 (0.2)	9.4 (3.4)	1.5 (0.2)	-5 (56)	1.0 (0.1)	3.1 (0.2)
F-NS	0.4 (0.2)	6.1 (1.2)	1.6 (0.1)	6 (56)	0.8 (0.1)	3.3 (0.3)

Table 2

Average and empirical standard deviation of parameter estimates over 25 repeated simulations. The models are fitted using 500 observations from a single realization, generated by a non-stationary model with smoothness $\nu = 0.5$.

Model	Parameters					
	ν	ρ_0	a_0	ψ_0 [°]	σ_0	σ_N [10^{-1}]
True	0.5	10	1	–	1	3.2
NF-S	1.0	5.3 (1.2)	1.5 (0.2)	15 (53)	0.9 (0.1)	3.4 (0.2)
NF-NS	1.0	7.5 (1.4)	1.6 (0.1)	-3 (46)	0.8 (0.2)	3.3 (0.3)
F-S	0.5 (0.2)	8.5 (3.0)	1.5 (0.2)	13 (53)	1.0 (0.2)	3.2 (0.2)
F-NS	0.6 (0.3)	6.6 (1.0)	2.1 (0.9)	17 (49)	0.9 (0.4)	3.5 (0.3)

B.2. Salinity data

Table 3

Average and empirical standard deviation of parameter estimates over 24 repetitions of holding out realizations from the salinity dataset.

Model	Parameters					
	ν	ρ_0 [km]	a_0	ψ_0 [°]	σ_0 [psu]	σ_N [10^{-2} psu]
NF-S	1.0	1.1 (0.3)	1.6 (0.2)	-73 (33)	1.3 (0.3)	0.1 (0.0)
NF-NS	1.0	1.7 (0.3)	1.5 (0.2)	-25 (26)	0.9 (0.1)	0.1 (0.0)
F-S	0.9 (0.2)	1.4 (0.8)	1.6 (0.2)	-69 (43)	1.3 (0.3)	0.1 (0.0)
F-NS	0.9 (0.3)	1.6 (0.6)	1.4 (0.2)	-14 (33)	0.9 (0.1)	0.1 (0.0)

B.3. Precipitation data

Table 4

Average and empirical standard deviation of parameter estimates over 26 repetitions of holding out realizations from the precipitation dataset.

Model	Parameters					
	ν	ρ_0 [°]	a_0	ψ_0 [°]	σ_0 [10^{-1} cm]	σ_N [10^{-2} cm]
NF-S	1.0	4.0 (0.1)	1.5 (0.2)	2 (10)	0.8 (0.0)	1.9 (0.0)
NF-NS	1.0	6.4 (1.8)	1.6 (0.5)	26 (13)	1.1 (0.2)	1.8 (0.1)
F-S	0.4 (0.1)	9.8 (0.5)	1.5 (0.2)	6 (16)	0.9 (0.0)	1.9 (0.0)
F-NS	0.4 (0.2)	5.5 (0.9)	1.6 (0.2)	30 (3)	0.8 (0.1)	1.8 (0.1)

References

Baker, Jr., G.A., Graves-Morris, P., 1996. Padé approximants. volume 59 of *Encyclopedia of Mathematics and its Applications*. Second ed., Cambridge University Press, Cambridge. URL: <https://doi.org/10.1017/CBO9780511530074>, doi:10.1017/CBO9780511530074.

Banerjee, S., Carlin, B.P., Gelfand, A.E., 2015. Hierarchical modeling and analysis for spatial data. volume 135 of *Monographs on Statistics and Applied Probability*. Second ed., CRC Press, Boca Raton, FL.

Baydin, A.I.m.G.s., Pearlmutter, B.A., Radul, A.A., Siskind, J.M., 2017. Automatic differentiation in machine learning: a survey. *J. Mach. Learn. Res.* 18, Paper No. 153, 43.

Berild, M.O., Fuglstad, G.A., 2023. Spatially varying anisotropy for Gaussian random fields in three-dimensional space. *Spat. Stat.* 55, Paper No. 100750, 32. URL: <https://doi.org/10.1016/j.spasta.2023.100750>, doi:10.1016/j.spasta.2023.100750.

Berild, M.O., Fuglstad, G.A., 2024. Non-stationary spatio-temporal modeling using the stochastic advection-diffusion equation. *Spat. Stat.* 64, Paper No. 100867, 22. URL: <https://doi.org/10.1016/j.spasta.2024.100867>, doi:10.1016/j.spasta.2024.100867.

Bolin, D., Kirchner, K., 2020. The rational SPDE approach for Gaussian random fields with general smoothness. *J. Comput. Graph. Statist.* 29, 274–285. URL: <https://doi.org/10.1080/10618600.2019.1665537>, doi:10.1080/10618600.2019.1665537.

Bolin, D., Simas, A.B., 2023. rSPDE: Rational Approximations of Fractional Stochastic Partial Differential Equations. URL: <https://CRAN.R-project.org/package=rSPDE>. r package version 2.3.3.

Bolin, D., Simas, A.B., Xiong, Z., 2024. Covariance-based rational approximations of fractional SPDEs for computationally efficient Bayesian inference. *J. Comput. Graph. Statist.* 33, 64–74. URL: <https://doi.org/10.1080/10618600.2023.2231051>, doi:10.1080/10618600.2023.2231051.

C3S, C.C.C.S., 2025. Climate reanalysis. URL: <https://climate.copernicus.eu/climate-reanalysis>.

Cressie, N., Wikle, C.K., 2011. Statistics for spatio-temporal data. Wiley Series in Probability and Statistics, John Wiley & Sons, Inc., Hoboken, NJ.

Damian, D., Sampson, P.D., Guttorp, P., 2001. Bayesian estimation of semi-parametric non-stationary spatial covariance structures. *Environmetrics: The official journal of the International Environmetrics Society* 12, 161–178.

Fuglstad, G.A., Lindgren, F., Simpson, D., Rue, H., 2015a. Exploring a new class of non-stationary spatial Gaussian random fields with varying local anisotropy. *Statist. Sinica* 25, 115–133.

Fuglstad, G.A., Simpson, D., Lindgren, F., Rue, H., 2015b. Does non-stationary spatial data always require non-stationary random fields? *Spat. Stat.* 14, 505–531. URL: <https://doi.org/10.1016/j.spasta.2015.10.001>, doi:10.1016/j.spasta.2015.10.001.

Fuglstad, G.A., Simpson, D., Lindgren, F., Rue, H., 2019. Constructing priors that penalize the complexity of Gaussian random fields. *J. Amer. Statist. Assoc.* 114, 445–452. URL: <https://doi.org/10.1080/01621459.2017.1415907>, doi:10.1080/01621459.2017.1415907.

Genton, M.G., Kleiber, W., 2015. Cross-covariance functions for multivariate geostatistics. *Statist. Sci.* 30, 147–163. URL: <https://doi.org/10.1214/14-STS487>, doi:10.1214/14-STS487.

Giles, M.B., 2008. Collected matrix derivative results for forward and reverse mode algorithmic differentiation, in: *Advances in automatic differentiation*. Springer, Berlin. volume 64 of *Lect. Notes Comput. Sci. Eng.*, pp. 35–44.

Heaton, M.J., Datta, A., Finley, A.O., Furrer, R., Guinness, J., Guhaniyogi, R., Gerber, F., Gramacy, R.B., Hammerling, D., Katzfuss, M., et al., 2019. A case study competition among methods for analyzing large spatial data. *Journal of agricultural, biological and environmental Statistics* 24, 398–425.

Higdon, D., 1998. A process-convolution approach to modelling temperatures in the north atlantic ocean. *Environmental and Ecological Statistics* 5, 173–190.

Ingebrigtsen, R., Lindgren, F., Steinsland, I., Martino, S., 2015. Estimation of a non-stationary model for annual precipitation in southern Norway using replicates of the spatial field. *Spat. Stat.* 14, 338–364. URL: <https://doi.org/10.1016/j.spasta.2015.07.003>, doi:10.1016/j.spasta.2015.07.003.

Kingma, D.P., Ba, J., 2017. Adam: A method for stochastic optimization. URL: <https://arxiv.org/abs/1412.6980>, arXiv:1412.6980.

Lilleborge, K., 2021. Bivariate Spatial Models using Stochastic Partial Differential Equations. Project thesis. Norwegian University of Science and Technology (NTNU).

Lindgren, F., 2024. fmesher: Triangle Meshes and Related Geometry Tools. URL: <https://inlabru-org.github.io/fmesher/>. r package version 0.1.7.9008, <https://github.com/inlabru-org/fmesher>.

Lindgren, F., Bolin, D., Rue, H., 2022. The SPDE approach for Gaussian and non-Gaussian fields: 10 years and still running. *Spat. Stat.* 50, Paper No. 100599, 29. URL: <https://doi.org/10.1016/j.spasta.2022.100599>, doi:10.1016/j.spasta.2022.100599.

Lindgren, F., Rue, H., Lindstrøm, J., 2011. An explicit link between Gaussian fields and Gaussian Markov random fields: the stochastic partial differential equation approach. *J. R. Stat. Soc. Ser. B Stat. Methodol.* 73, 423–498. URL: <https://doi.org/10.1111/j.1467-9868.2011.00777.x>, doi:10.1111/j.1467-9868.2011.00777.x. with discussion and a reply by the authors.

Llamazares-Elias, L., Latz, J., Lindgren, F., 2024. A parameterization of anisotropic gaussian fields with penalized complexity priors. URL: <https://arxiv.org/abs/2409.02331>, arXiv:2409.02331.

Minka, T.P., 2000. Old and new matrix algebra useful for statistics URL: <https://tminka.github.io/papers/matrix/>.

Neto, J.H.V., Schmidt, A.M., Guttorp, P., 2014. Accounting for spatially varying directional effects in spatial covariance structures. *Journal of the Royal Statistical Society Series C: Applied Statistics* 63, 103–122.

Nytko, N., Taghikhakhshi, A., Zaman, T.U., MacLachlan, S., Olson, L.N., West, M., 2023. Optimized sparse matrix operations for reverse mode automatic differentiation. URL: <https://arxiv.org/abs/2212.05159>, arXiv:2212.05159.

Paciorek, C.J., Schervish, M.J., 2006. Spatial modelling using a new class of nonstationary covariance functions. *Environmetrics: The official journal of the International Environmetrics Society* 17, 483–506.

Paszke, A., Gross, S., Massa, F., Lerer, A., Bradbury, J., Chanan, G., Killeen, T., Lin, Z., Gimelshein, N., Antiga, L., Desmaison, A., Köpf, A., Yang, E., DeVito, Z., Raison, M., Tejani, A., Chilamkurthy, S., Steiner, B., Fang, L., Bai, J., Chintala, S., 2019. Pytorch: An imperative style, high-performance deep learning library. URL: <https://arxiv.org/abs/1912.01703>, arXiv:1912.01703.

Risser, M.D., Calder, C.A., 2015. Regression-based covariance functions for nonstationary spatial modeling. *Environmetrics* 26, 284–297.

Risser, M.D., Calder, C.A., 2017. Local likelihood estimation for covariance functions with spatially-varying parameters: the convospat package for r. *Journal of Statistical Software* 81, 1–32.

Risser, M.D., Turek, D., 2020. Bayesian inference for high-dimensional nonstationary gaussian processes. *Journal of Statistical Computation and Simulation* 90, 2902–2928.

Rue, H., Martino, S., 2007. Approximate Bayesian inference for hierarchical Gaussian Markov random field models. *J. Statist. Plann. Inference* 137, 3177–3192. URL: <https://doi.org/10.1016/j.jspi.2006.07.016>, doi:10.1016/j.jspi.2006.07.016.

Sampson, P.D., 2010. Constructions for nonstationary spatial processes, in: *Handbook of spatial statistics*. CRC/Press, pp. 119–130.

Sampson, P.D., Guttorp, P., 1992. Nonparametric estimation of nonstationary spatial covariance structure. *Journal of the American Statistical Association* 87, 108–119.

Schmidt, A.M., Guttorp, P., 2020. Flexible spatial covariance functions. *Spatial Statistics* 37, 100416.

Schmidt, A.M., O'Hagan, A., 2003. Bayesian inference for non-stationary spatial covariance structure via spatial deformations. *Journal of the Royal Statistical Society Series B: Statistical Methodology* 65, 743–758.

Simpson, D., Rue, H., Riebler, A., Martins, T.G., Sørbye, S.H., 2017. Penalising model component complexity: a principled, practical approach to constructing priors. *Statist. Sci.* 32, 1–28. URL: <https://doi.org/10.1214/16-STS576>, doi:10.1214/16-STS576.

SINTEF, 1987. Sinmod. URL: <https://www.sintef.no/programvare/sinmod/>. accessed: 2025-03-07.

Slagstad, D., McClamans, T.A., 2005. Modeling the ecosystem dynamics of the barents sea including the marginal ice zone: I. physical and chemical oceanography. *Journal of Marine Systems* 58, 1–18. URL: <https://www.sciencedirect.com/science/article/pii/S0924796305001296>.

Stein, M.L., 1999. *Interpolation of spatial data: some theory for kriging*. Springer Science & Business Media.

Takahashi, K., 1973. Formation of sparse bus impedance matrix and its application to short circuit study, in: Proc. PICA Conference, June, 1973.

Talley, L.D., 2011. *Descriptive Physical Oceanography: An Introduction*. Academic Press.